

Flow control of three-dimensional cylinders transitioning to turbulence via multi-agent reinforcement learning

P. Suárez^a, F. Álcantara-Ávila^a, J. Rabault^b, A. Miró^c, B. Font^d, O. Lehmkuhl^c, R. Vinuesa^a

^a*FLOW, Engineering Mechanics, KTH Royal Institute of Technology, Stockholm, Sweden*

^b*Independent researcher, Oslo, Norway*

^c*Barcelona Supercomputing Center, Barcelona, Spain*

^d*Faculty of Mechanical Engineering, Technische Universiteit Delft, The Netherlands*

Abstract

Designing active-flow-control (AFC) strategies for three-dimensional (3D) bluff bodies is a challenging task with critical industrial implications. In this study we explore the potential of discovering novel control strategies for drag reduction using deep reinforcement learning. We introduce a high-dimensional AFC setup on a 3D cylinder, considering Reynolds numbers (Re_D) from 100 to 400, which is a range including the transition to 3D wake instabilities. The setup involves multiple zero-net-mass-flux jets positioned on the top and bottom surfaces, aligned into two slots. The method relies on coupling the computational-fluid-dynamics solver with a multi-agent reinforcement-learning (MARL) framework based on the proximal-policy-optimization algorithm. MARL offers several advantages: it exploits local invariance, adaptable control across geometries, facilitates transfer learning and cross-application of agents, and results in a significant training speedup. For instance, our results demonstrate 21% drag reduction for $Re_D = 300$, outperforming classical periodic control, which yields up to 6% reduction.

Email addresses: polsm@kth.se (P. Suárez), rvinuesa@mech.kth.se (R. Vinuesa)

To the authors' knowledge, the present MARL-based framework represents the first time where training is conducted in 3D cylinders. This breakthrough paves the way for conducting AFC on progressively more complex turbulent-flow configurations.

Keywords: Fluid mechanics, Drag reduction, Deep learning, Active flow control, Multi-agent Reinforcement learning

Introduction

The transportation industry, and the aerospace sector in particular, require new ground-breaking methods to overcome the challenges that they are currently facing, *i.e.* the need to reduce fossil-fuel-related emissions. The implementation of flow-control systems, both passive and active, plays a vital role in the development of more sustainable solutions that can drastically reduce fuel usage, mitigate air and noise pollution, and even improve maneuverability [1]. The aerodynamic drag in subsonic aircraft is divided mainly into pressure, skin friction (due to viscous stresses), and lift-induced components. Wing-tip effects aside, the two former are the dominant terms.

Control devices utilize aerodynamic principles to manipulate pressure and viscosity, effectively reducing drag. For instance, slats and flaps are control surfaces located on the leading and trailing edges of an airfoil which impact the aircraft operational conditions [2]. Modern advancements include winglets [3] aimed at mitigating the lift-induced drag or vortex generators [4], which are used to control boundary-layer separation. Such developments have significantly improved aerodynamic performance. Additionally, a number of alternative approaches like morphing surfaces, spiroids, or blowing devices [5, 6] are currently being explored. Despite their extensive potential, designing optimal geometries or strategies for these devices

has raised significant challenges due to the massive computational resources required to tackle such an intricate interplay between pressure and viscous effects in all flight regimes. Nevertheless, ongoing research efforts and current computational innovations are leading to further advancements toward achieving optimal global control.

In parallel with the recent innovations in flow control, the irruption of machine-learning (ML) techniques has brought tremendous potential to the aeronautics industry, both in terms of studying fundamental problems in fluid mechanics [7, 8] and devising completely new strategies for active and passive flow control (AFC and PFC, respectively) [9]. Deep reinforcement learning (DRL) is one of the fastest-growing fields within ML [10] and one of the techniques attracting most interest. Expanding on its success in tabletop games [11], DRL works well in any system where a controller interacts with an environment to improve a task. That is the case for most AFC cases since DRL interacts with the flow on the fly and receives feedback from it, gaining experience and progressively improving the choice of actions.

AFC setups are complex high-dimensional problems that require substantial computational resources to find the optimal values within the large parametric space of the control system. DRL and neural networks have emerged as valuable tools to make this process feasible, enabling the development of effective control strategies at a reasonable computational cost. The literature on DRL for AFC grows at a fast pace, exhibiting studies on flow control for two-dimensional (2D) cylinders ranging from $Re_D = 100$ and 2000 (where Re_D is the Reynolds number based on inflow velocity U_∞ and cylinder diameter D) with 17% and 38% drag reduction, respectively [12, 13, 14, 15, 16, 17, 18], aircraft wings [19], fluid-structure interaction [20], turbulent channels [21], shape optimization [22, 23, 24], Rayleigh–

Bénard convection [25] or turbulence modelling [26, 27, 28, 29]. Some recent literature demonstrates the possibility of transfer learning from exploration done in 2D cylinders to 3D domains and higher Re_D : in Ref. [30] the wake of a cylinder is controlled by means of two rotating cylinders and in Ref. [18] the control is carried out through multiple jets over the cylinder surface. The present work extends this state-of-the-art in 3D cylinders, considering multiple actuators governed by the novel implementation of a multi-agent reinforcement learning (MARL) framework into a setup based on a distributed-input distributed-output (DIDO) scheme. In our case, the agent focuses on exploring the underlying 3D physics during training, and the AFC is implemented by multiple independent zero-net-mass-flow (ZNMF) jets placed along the cylinder span and aligned along two slots on the top and bottom surfaces. To the best of the authors’ knowledge, this work marks the first time where exploration sessions are directly conducted within 3D cylinders.

As the Reynolds number increases, the flow around a cylinder exhibits different characteristics. Initially, up to approximately $Re_D \approx 40$, steady laminar flow prevails, characterized by symmetric counter-rotating vortices in the near wake. Beyond $Re_D \approx 190$, laminar vortex shedding emerges, forming the well-known Kármán vortex street. In the subsequent regimes, between $190 < Re_D < 260$, the mode-A instability, characterized by dominant spanwise wavelengths of $\lambda_z = 4D$ [31, 32] is dominant. As $Re_D \approx 260$ is surpassed, mode B becomes predominant, and finer three-dimensional features with shorter wavelengths of $\lambda_z = 1D$ are found. Beyond these regimes, the cylinder wake evolves into a more chaotic and turbulent state.

Discovering flow-control strategies for the flow around a cylinder when the wake transitions from 2D to 3D is challenging. The MARL setup needs to exploit the characteristics of the spanwise structures as the wake be-

comes three-dimensional to devise effective control approaches. The transition range of for 2D environments has been shown to be suitable, showcasing the generalization ability of deep neural networks [12]. However, it has been widely recognized that studying $Re_D > 250$ in a 2D context leads to inaccurate predictions of aerodynamic forces. In the present work, the exploration of the 3D context allows tackling possible novel strategies that take advantage of the drag reduction originated by 3D instabilities.

DRL is based on maximizing a reward (R) provided to an agent interacting continuously with an environment through actions A . The agent receives information about the environment state at each actuation step through partial observations S of the system. A sequence of consecutive actions is denoted as an episode. When a batch of episodes is finished, the agent updates the neural-network weights to progressively determine a policy that maximizes the expected reward for a given S . For a detailed understanding of the most recent advances in flow control with MARL we refer to Refs. [33, 34].

Results

This study presents our findings on high-dimensional distributed forcing using multiple jets aligned along the spanwise direction of a 3D infinite cylinder. Training was carried out using multi-agent reinforcement learning (MARL), which demonstrates superior performance compared to conventional single-agent reinforcement learning (SARL) methods. In the subsequent sections, we explore the development of training strategies aimed at achieving high rewards. We then evaluate the optimal model and compare it with the classical periodic-control study (PC). Additionally, we investigate the utilization of the trained agents for exploitation without involving any exploration. Statistical analyses are conducted to elucidate the underlying physical mechanisms responsible for drag reduction, thereby leading to potential energy savings.

Training

To ensure an effective DRL training process, it is crucial to precisely define rewards, penalties, action ranges, and a representative environment state. A fundamental aspect of training is leveraging the physical understanding of the controlled phenomenon to evaluate anticipated reward values and physical control strategies thoughtfully. With these considerations in mind, Figure 1(a) shows the training curves for the four investigated cases in this study, at Reynolds numbers $Re_D = 100, 200, 300,$ and 400 . Commonly, sequences of actions A , states S , and rewards R are referred to as “environment episodes”. However, in this case, it is more appropriate to call them “pseudo-environment episodes” due to the difference between SARL and MARL, where MARL involves multiple pseudo-environments within an environment. Hence, this Figure shows all the final rewards from the raw

pseudo-environments, together with the pure drag reduction and lift-biased penalization contributions (see the Methods section for more details). As an example, the $Re_D = 300$ scenario closely resembles the ideal training condition. This is because the curves exhibit minimal lift bias (see the Methods section) and result in a total reward that matches the pure drag reduction, stabilizing at R values that are manageable and simple to track. Similar patterns are obtained for the other Re_D cases indicating that the discovered policies are promising for all the cases. Note that we also observe several instances of apparent unlearning such as for $Re_D = 400$ at the episode 500 approximately. This is due to additional exploration of the agent, aimed at increasing the lift asymmetry (note the decrease of the blue line), but quickly returning to exploiting what the agent has identified as a well-performing policy. Once the reward value settles around a certain converged value of $R \approx 1.0$, the training process is concluded. Then, we proceed to the assessment of the learned policies in deterministic mode, which is discussed next.

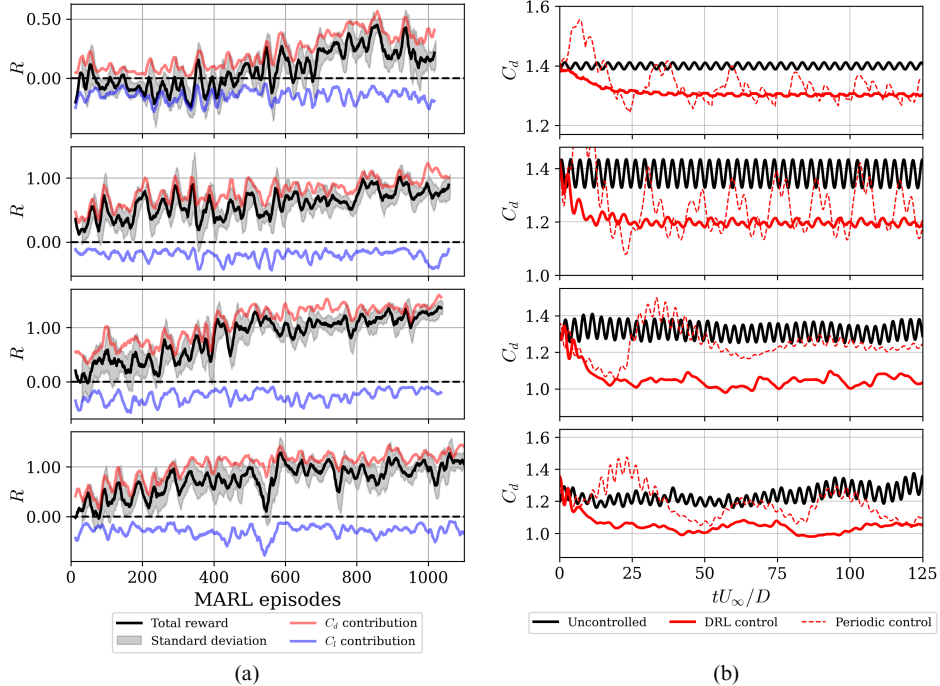


Figure 1: **Reward evolution during exploration episodes and exploitation of the policies.** (a) Final total reward R together with its lift-bias and pure drag-reduction contributions during exploration in training sessions. Signals are smoothed by a moving average of 15 values, and the grey shaded area corresponds to the minimum and maximum rewards over those 15 episodes. (b) Drag-coefficient evolution during exploitation of the model. Comparison between uncontrolled, DRL control and PC. From top to bottom, $Re_D = 100, 200, 300$ and 400 .

In terms of computational cost, training is the most significant part. On average, each training session requires about 1200 MARL episodes, which is equivalent to running 120 numerical simulations for the entire domain. All exploration sessions were conducted on the Dardel high-performance computer in the PDC Center at KTH Royal Institute of Technology. The sessions run on 8 nodes simultaneously, each running one numerical simu-

lation comprising 10 simultaneous pseudo-environments. Hence, 80 pseudo-environments in total. Each node has two AMD EPYC™ Zen2 2.25 GHz 64-core processors with 512 GB memory. With each batch of 8 simulations taking ideally five hours in this particular architecture, it requires less than four days of continuous operation. Moreover, as the Reynolds number (Re_D) increases, the computational cost increases significantly.

Exploitation of the models

At this point, the agent policies are evaluated without any exploration. As a result, the agent calculates the most likely value of the action A within its learned probability distribution, aiming to maximize the expected reward. In Figure 1(b) we show the temporal evolution of the DRL control and the PC. The DRL-based control exhibits a clear two-phase process that starts with a short transient period followed by the stationary control policy. We included the transition phase between $t = 0$ to around 20 convective time units. Note that the vortex-shedding period is $T_k = 1/St \approx 1/0.2 = 5$, where $St = fD/U_\infty$ is the Strouhal number and f is the vortex-shedding frequency. These results imply that it takes less than $4T_k$ to reach the stationary behavior. The DRL-based control exhibits a first suction/ejection overshoot which destabilizes the wake, and then it proceeds to re-stabilize it in a second phase. During the latter, the jet mass flux exhibits lower values which barely reach 75% of those in the transient overshoots.

This control strategy persists until control stabilizes into stationary behavior, which is monitored by assessing mean quantities and fluctuations in aerodynamic forces. The averaged drag-reduction results for all Re_D are reported in Figure 2(a). It is important to note that all the cases lead to effective drag-reduction rates. The overall performance is much better

than what can be obtained with the classical PC strategies. The values are averaged in time by considering an interval of at least $20T_k$, *i.e.* over 100 time units, excluding the transients obtained after applying the control. The root-mean-square of the fluctuations, $\text{RMS} = \sqrt{(1/n) \sum_{i=1}^n (x_i - \bar{x})^2}$, minimum and maximum values provide deeper insights into the mentioned robustness. While the mean values alone may suggest a good performance of the PC, the merits of the control should not be assessed solely based on this quantity. When considering an optimal control strategy, the preferred choice typically involves selecting a control with minimal variability and few extreme values, which are characteristics exhibited as evidenced by the DRL-based control.

We also study the ratio between the total fluid mass intercepted by the frontal area of the cylinder E_∞ and the total mass used by the actuators E_c . Based on the definitions used in Ref. [18], we propose the following expression for the ratio E_c^* :

$$E_c^* = \frac{E_c}{E_\infty} = \frac{L_{\text{jet}}}{(t_2 - t_1)Q_\infty L_z} \int_{t_1}^{t_2} \sum_{i=1}^{n_{\text{jets}}} |Q_i(t)| \, dt, \quad (1)$$

where t_1 and t_2 define the start and end of our time interval for evaluating the control. Note that a complete evaluation of the mass used by the actuators would depend on the actual jets used in the experimental setup, and in this work we adopt a purely numerical approach based on modifying the Dirichlet boundary condition at the cylinder surface. Keeping this aspect in mind, the present numerical work shows that the mass cost is minimal compared to the gains achieved through drag reduction. The results in Figure 2 for $E_c^*/\Delta C_d$ (which is the change in the drag coefficient) highlight how DRL-based control strategies require only half as much mass as that required by

the classical control.

We provide additional physical insight by assessing the power-spectral density (PSD) of the streamwise velocity, shown in Figure 2(b). This figure illustrates how the change of frequency impacts the wake topology after applying the various control strategies. In particular, both the DRL-based control and PC cases exhibit a reduction in St . Further insight into the various control strategies is provided in Figure 2(c), where several characteristic variables of the various controls are shown. The first important observation is the fact that the root-mean-square (RMS) of the jet mass-flow rate (computed by averaging in time and the spanwise direction) is one order of magnitude lower in the DRL than in the PC. This indicates that the DRL-based control strategies lead to more stable and robust configurations, avoiding large peak-to-peak variations in the actuation. Also, note that we show the control frequencies f_c for the PC (where we report the optimal control frequency) and the DRL (where we report the dominant frequency). Although the f_c values are not dramatically different in the PC and DRL cases, the latter exhibit significantly more complex control laws than the former. It is worth noting that we conducted a parametric study to assess the optimal values of f_c and Q for classical PC, as discussed in the Methods section.

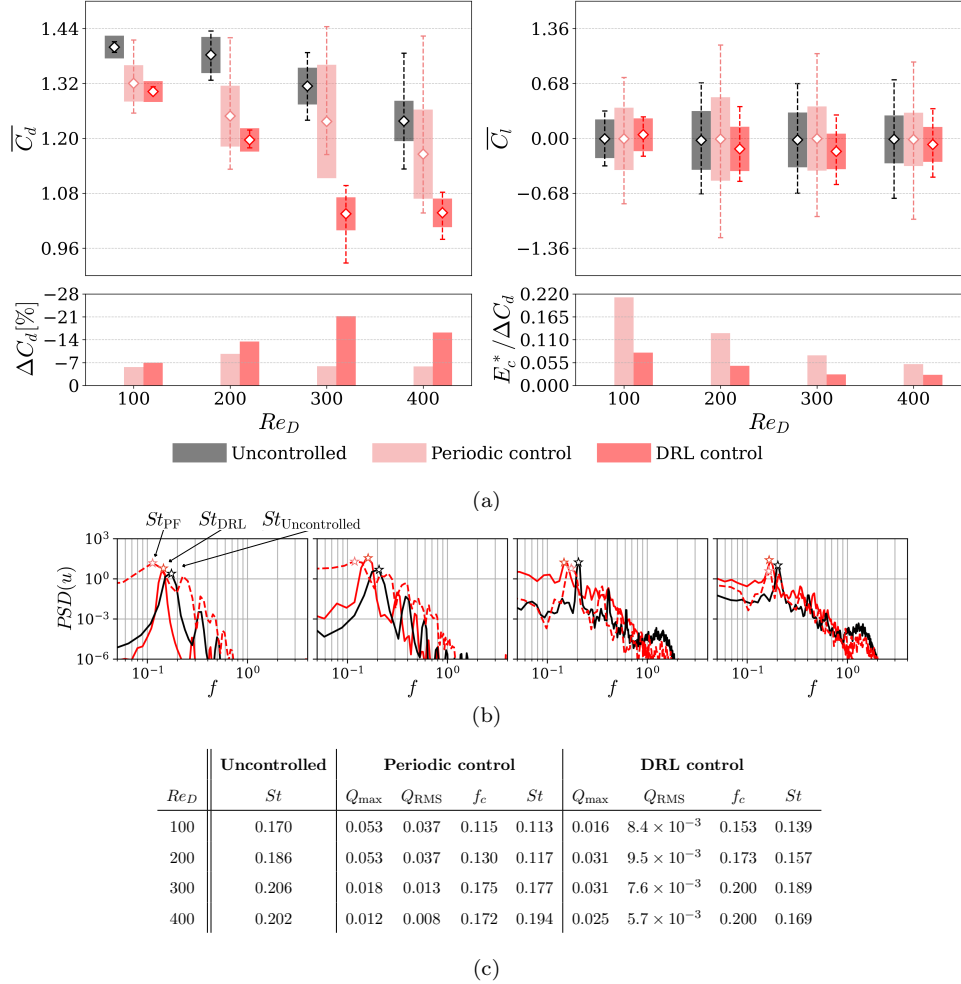


Figure 2: **Summary of aerodynamic forces, wake spectra and mass-flow rate characteristics for the various controls.** (a) Mean drag (C_d) and lift (C_l) coefficients shown as white diamonds, RMS of fluctuations are represented as thick bars, and maximum-minimum shown as dashed intervals for each case. Summary of percentage drag reduction ΔC_d , and non-dimensionalized cost metric per drag reduction rate $E_c^*/\Delta C_d$ (lower is better), as defined in Equation (1). (b) Power-spectral density of the streamwise velocity u evaluated at the streamwise location $x/D = 10.5$ for uncontrolled (black), PC (red dashed) and DRL-based control (red). From left to right, $Re_D = 100, 200, 300$ and 400 . (c) Main characteristics that define different control strategies, including the Strouhal number St , maximum and fluctuations RMS of mass-flow rates per unit width (Q_{\max} and Q_{RMS}) and control frequency f_c (we find the optimum value for PC and report the dominant frequency for DRL).

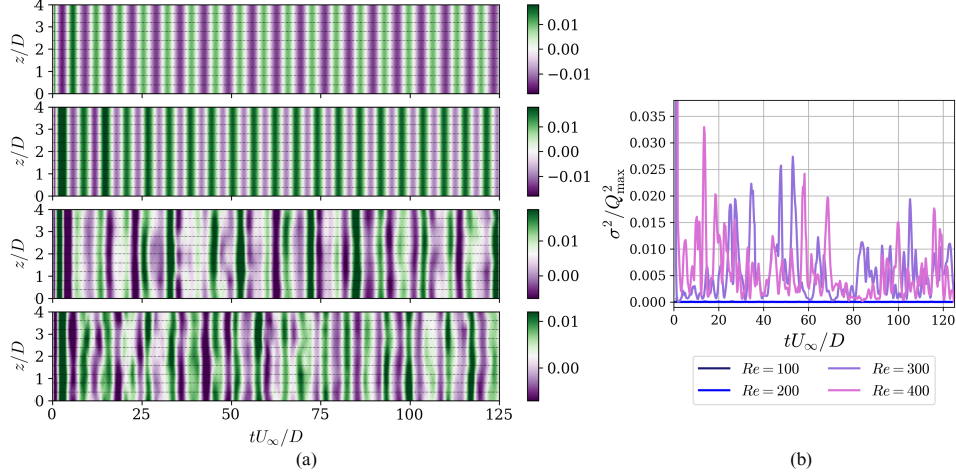


Figure 3: **Evolution of the mass-flow rate associated with the jets in time and in the spanwise direction.** (a) Mass-flow rate per unit width Q as a function of time for all jets individually, showing also their spanwise distribution for the DRL cases. From top to bottom: $Re_D = 100, 200, 300$ and 400 . (b) Evolution in time of the variance of the mass-flow rate computed in z , $\sigma^2(t) = (1/n_{\text{jets}}) \sum_{i=1}^{n_{\text{jets}}} (Q_i(t) - \bar{Q}(t))^2$, for the different Reynolds numbers under study. Note that σ^2 is normalized by the squared peak Q values from each case, and $\sigma^2 = 0$ is obtained for $Re = 100$ and 200 .

Figure 3 demonstrates the biggest advantage of a MARL implementation: the control policy can act locally, exploiting wake vortical structures and distributing the flow of the jets in the spanwise direction to maximize the global objective of minimizing the overall drag. In Figure 3(a), we display the temporal and spanwise evolution of the mass-flow rate per unit length from the jets when considering the DRL-based control strategy. The agent utilizes less than 10% of the maximum possible value, as discussed in the Methods section. While cases up to $Re_D = 200$ exhibit a uniform distribution in the spanwise direction, beyond this Reynolds number, the control exhibits spanwise variations. This is further supported by the re-

sults in Figure 3(b), which shows the instantaneous variance of the mass flow rate distributed in z as a function of time for the various cases, denoted as σ^2 . As mentioned in the Introduction, for $Re_D \geq 250$ the wake displays three-dimensional features, effectively utilized by the DRL control to maximize the achieved drag-reduction rates. During the exploration stage, for $Re_D = 100$ and 200 , the agent could not find any strategy with spanwise variations leading to better performance, indicating that the wake is two-dimensional in these cases, favoring spanwise-uniform control strategies. On the other hand, at $Re_D = 300$ and 400 , it is possible to observe patterns in the flow related to the transitional Re_D , including spanwise structures of approximately one cylinder diameter ($\lambda_z = 1D$) associated with mode-B instabilities. Also note that a basic SARL approach does not effectively utilize these local spanwise length scales, and the MARL setup enables to exploit structures in the spanwise direction, as evidenced by the non-zero values of the variance of the control in z .

In Figure 4 we illustrate how the flow topology is influenced by the various drag-reduction strategies, on three representative phases: uncontrolled, transient, and stabilized control. The flow visualizations indicate that the control strategies based on DRL aim to enhance the spacing between successive vortical structures, resulting in a reduction of the vortex-shedding period T_k . Hence, mode-B instabilities are diminished when the control is applied, and the intensity of the vortex shedding is attenuated. These changes lead to a more organized wake structure, resembling the characteristic two-dimensional laminar wake. Figures 1(b) and 2(a) corroborate these findings, illustrating diminished oscillations during the controlled phase.

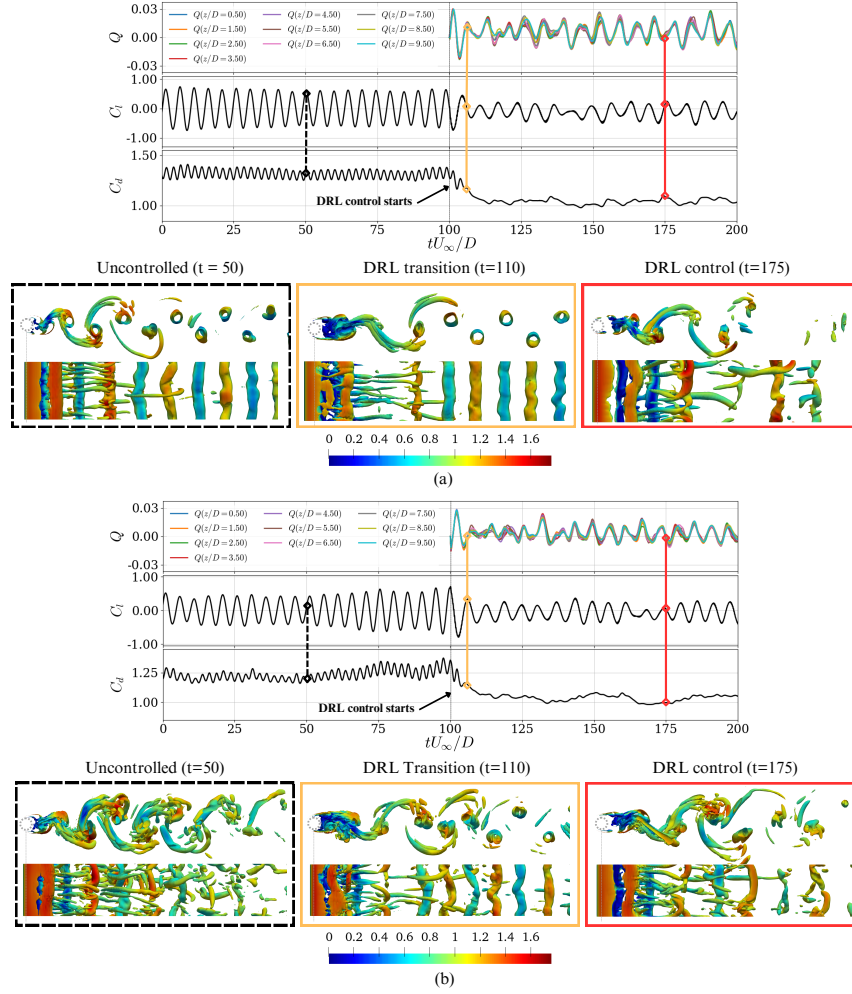


Figure 4: **Visualizations of the flow coherent structures during DRL-based strategy exploitation.** Temporal evolution of the flow at (a) $Re_D = 300$ and (b) $Re_D = 400$, from uncontrolled state to a stable DRL control. (Top) Non-dimensional mass-flow rate per unit width Q , lift coefficient C_l and drag coefficient C_d as a function of time; (bottom) snapshots showing vortical structures identified with the λ_2 criterion [35], where the isosurface $\lambda_2 D^2 / U_\infty^2 = -0.5$ is shown for uncontrolled, transient, and DRL-controlled states. The colors framing the flow visualizations correspond to the instants indicated in the temporal evolution of the relevant flow quantities.

Studying flow statistics offers deeper insight into the mechanisms employed by the DRL agent to discover flow-control strategies, particularly when analyzing the mean flow and the Reynolds stresses. To compute the latter, the Reynolds decomposition is used to decompose the flow variables (u) into time-averaged mean (\bar{u}) and fluctuating (u') components, $u = \bar{u} + u'$. In Figures 5(a)–(c), we observe the impact of the DRL-based control: the wake nearly doubles the recirculation-bubble length, delaying the wake-stagnation point by approximately one diameter in the streamwise direction. Instead of showing all cases, we only present $Re_D = 400$ as a representative case. Figures 5(d) and 5(e) show how the wake also changes noticeably, being slightly wider but decaying much faster as we move downstream. Note that peaks in v fluctuations follow the same pattern, meaning that the counter-rotating vortices occur further as well. The pressure coefficient $C_p = 2(P - P_\infty)/(\rho U_\infty^2)$ around the cylinder is shown in Figure 5(f) for the DRL-controlled case and the uncontrolled one. The back pressure increases by $\Delta \overline{C_p^b} \approx 0.4$, which is directly related to the drag reduction mechanism.

The Reynolds stresses are presented in Figure 5(g), which shows that the peaks move downwards in the streamwise direction after applying the control, with only small changes in the vertical location. Additional analysis is provided in Figure 5(h), where the DRL-based control generally leads to the reduction of the peak magnitude in almost all the fluctuating quantities. In this case, all Re_D values are presented to elucidate that the same behavior occurs within this regime range. When considering fluctuations in the spanwise direction w' , we notice a distinct pattern: an increase occurs at $Re_D = 300$, while a decrease is observed at higher Re_D values.

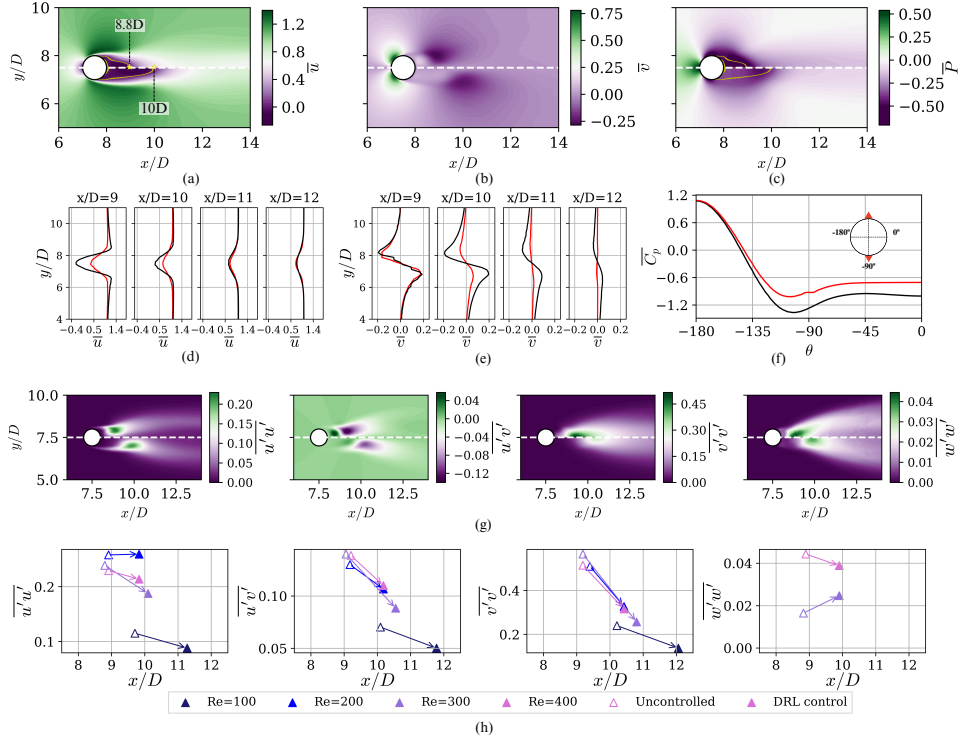


Figure 5: **Mean flow and Reynolds stresses for the DRL-controlled cases.** (a)–(c) Mean velocities and pressure fields for $Re_D = 400$, where (top) is uncontrolled and (bottom) is DRL-controlled flow. Yellow lines denote the regions where $\bar{u} = 0$ which indicate the wake-stagnation points also annotated with their x/D location. (d)–(f) Mean wake profiles of \bar{u} and \bar{v} , as well as mean pressure distribution \bar{P} on the cylinder, respectively. We show (black) uncontrolled and (red) controlled cases. (g) Reynolds stresses $\overline{u'u'}$, $\overline{u'v'}$, $\overline{v'v'}$ and $\overline{w'w'}$, where (top) is uncontrolled and (bottom) is DRL-controlled flow. (h) Peak values for Reynolds stresses and their x/D locations for all the Reynolds numbers under study. Note that $\overline{w'w'}$ for $Re_D = 100$ and 200 is not displayed because it is zero.

Discussion and conclusions

In this study a multi-agent reinforcement-learning (MARL) framework is coupled with a numerical solver to discover effective drag-reduction strategies by controlling multiple jets placed along the span of three-dimensional cylinders. We study cases at $Re_D = 100, 200, 300,$ and 400 , where wake transition from 2D to 3D is observed. All DRL-based control policies outperform the classical periodic control in this Re_D range. This is characterized by the emergence of spanwise instabilities, which the DRL agent can exploit to discover effective drag-reduction strategies. This is achieved by taking advantage of exploiting the underlying physics within pseudo-environments and optimizing the global problem involving multiple interactions in parallel. One of the main advantages of employing MARL is the capability to deploy trained agents across various cylinder lengths and numbers of actuators while ensuring consistency in the spanwise width of the jets (L_{jet}) and their corresponding pressure values as observation states (S). Note that the training focuses on symmetries and invariant structures. This would not be possible with SARL, which is restricted to a certain number of actuators (and also the corresponding algorithm limitations). MARL allows for cheaper training sessions in smaller and simplified computational domains, thereby speeding up the process, which is required to perform flow control in high-fidelity simulations.

These findings highlight the effectiveness of the DRL approach, which can discover flow-control strategies more sophisticated than those obtained with the classical periodic control, spanning wide ranges of frequencies and tackling different flow features in the wake. DRL-based control achieves a remarkable performance, reducing drag by 21% and 16.5% for $Re = 300$

and 400 respectively, outperforming PC strategies which only achieve around 6% reduction for both Re . Furthermore, the results presented here represent the first training conducted in 3D cylinders using a MARL implementation. This sets a new benchmark for the DRL community, which may motivate its use in future applications for DIDO schemes.

Methods

Problem configuration and numerical setup

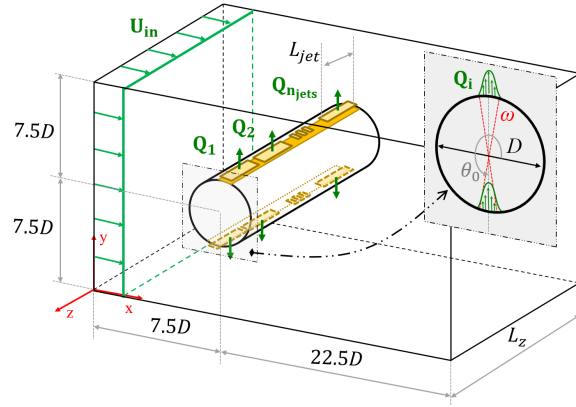
The present study consists of a 3D cylinder exposed to a constant inflow in the streamwise direction. All domain lengths are non-dimensional, using the cylinder diameter D as the reference length. The geometry under consideration is presented in Figure 6(a). The computational domain has a streamwise length of $L_x = 30D$, a height of $L_y = 15D$, and a spanwise length of $L_z = 4D$. The cylinder is centered at $(x, y) = (7.5D, 7.5D)$. Since the cylinder is considered to be infinitely long in the spanwise direction, we use periodic boundary conditions in z . Furthermore, we use a Dirichlet condition with a constant velocity U_∞ at the inlet. The top, bottom and outflow surfaces are outlets with imposed zero velocity gradient and constant pressure. The cylinder surfaces have no-slip and no-penetration conditions with zero velocity. The coordinate-system origin is located at the front-face left-bottom corner. The last boundary conditions correspond to the cylinder actuators which enable the control. The cylinder has a total of two sets of $n_{\text{jet}} = 10$ aligned synthetic jets that extend along its entire spanwise dimension, with a spanwise width $L_{\text{jet}} = 0.4D$. Each set is placed at the top and bottom of the cylinder (at $\theta_0^{\text{top}} = 90^\circ$ and $\theta_0^{\text{bottom}} = 270^\circ$, respectively), defined as independent boundaries. The mass-flow rate can

be changed by external actors (the DRL agent in this case, as discussed below). These actuators have an arc length in the xy plane of $\omega = 10^\circ$ and no gap between the jets in z is considered. The jet-velocity profile is defined in terms of the angle θ and the desired mass-flow rate Q per unit width:

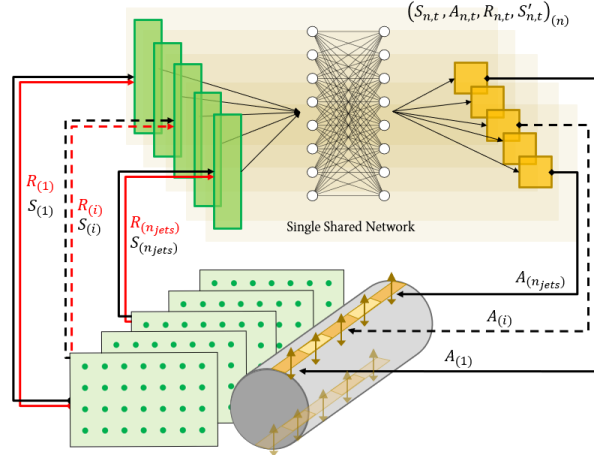
$$\|U(Q, \theta)\| = Q \frac{\pi}{\rho D \omega} \cos\left(\frac{\pi}{\omega}(\theta - \theta_0)\right), \quad (2)$$

where $Q = \dot{m}/L_z$ and $|\theta - \theta_0| \in [-\omega/2, \omega/2]$, \dot{m} is the mass flow rate. The absolute value of the jet velocity is projected into the x and y axes, since $\|U_{\text{jet}}\|$ corresponds to the radial cylinder direction. For each pseudo-environment, we set opposite action values within the pair of top and bottom jets *i.e.* $Q_{90^\circ} = -Q_{270^\circ}$, in order to ensure the global zero net mass flux. An earlier version of this setup was developed in Ref. [36].

A conceptually similar control approach was reported in Ref. [37], in particular the one they denote as *out-phase*. Out-phase approach consists of different constant mass-flow sinusoidal distributions along the spanwise with different wavelengths.



(a)



(b)

Figure 6: **Conceptual visualization of the computational domain and the MARL framework.** (a) Schematic representation of the computational domain with cylinder diameter D as the reference length. Here ω is the jet width and θ_0 is the angular location of each jet. In green, we show the velocity condition for the inlet U_∞ and the sinusoidal profile in the jet azimuthal direction. Note that this representation is not to scale. (b) MARL framework applied to a three-dimensional cylinder equipped with distributed input distributed output (DIDO). Note that is a schematic representation, and the S slices are not to scale.

The transition from laminar to the emergence of first three-dimensional instabilities in the cylinder wake occurs within a range of $Re_D = 200$ and 300 [31, 38, 39, 40, 41, 42]. The motivation of this research is to challenge the control system to discover the optimal strategies as the flow starts to become three-dimensional. By being able to manipulate scales with different spanwise wavelengths in the wake, the DRL-based control can learn effective mechanisms leading to a substantial reduction of the drag in the cylinder.

The numerical simulations are carried out by means of the numerical solver Alya, which is described in detail in Ref. [43]. The spatial discretization is based on the finite-element method (FEM) and the incompressible Navier–Stokes equations:

$$\partial_t \mathbf{u} + (\mathbf{u} \cdot \nabla) \mathbf{u} - \nabla \cdot (2\nu \boldsymbol{\epsilon}) + \nabla p = \mathbf{f}, \quad (3)$$

$$\nabla \cdot \mathbf{u} = 0, \quad (4)$$

are integrated numerically, where $\boldsymbol{\epsilon}$ is a function of the velocity \mathbf{u} which defines the velocity strain-rate tensor $\boldsymbol{\epsilon} = 1/2(\nabla \mathbf{u} + (\nabla \mathbf{u})^T)$ and \mathbf{f} are the external body forces. In Equation (4), the convective term $(\mathbf{u} \cdot \nabla) \mathbf{u}$ is expressed as a term conserving energy, momentum and angular momentum [44, 45]. For the time discretization, a semi-implicit method is used where the convective term follows a second-order Runge–Kutta scheme and a Crank–Nicholson scheme is used for the diffusive term [46]. To select the appropriate time step, Alya uses an eigenvalue-based time-integration scheme [47]. Then, for each time step, the numerical solution of these equations is computed. Drag and lift forces (F_x and F_y , respectively) forces are obtained by integration over the cylinder surface \mathbf{s} :

$$\mathbf{F} = \int (\boldsymbol{\varsigma} \cdot \mathbf{n}) \cdot \mathbf{e}_j ds, \quad (5)$$

where $\boldsymbol{\varsigma}$ is the Cauchy stress tensor, \mathbf{n} the unit vector normal to the surface and \mathbf{e}_j is a unit vector with the direction of the main flow velocity for F_x and the perpendicular cross-flow direction to it for F_y .

Multi-agent reinforcement learning (MARL)

In the present work, we implemented a deep-reinforcement-learning (DRL) framework using Tensorforce libraries [48]. DRL is very well suited for unsteady flow-control problems as it provides the possibility to dynamically interact with an environment, being able to dynamically set the actuation based on the varying flow state. We use the proximal-policy-optimization (PPO) algorithm [49], which is a policy-gradient approach based on a surrogate loss function for policy updates to prevent drastic drops in performance. This algorithm demonstrates robustness, as it is somewhat forgiving with hyperparameter initializations and can perform adequately across a diverse range of RL tasks without extensive tuning.

The neural-network architecture consists of two dense layers of 512 neurons each. The batch size, *i.e.* the total number of experiences that the PPO agent uses for each gradient-descent iteration, is set to 80, which is larger than the typical values used in 2D trainings [50, 51], but sufficiently small to efficiently update the neural-network parameters. If there is a discrepancy between the batch size and the environments running at the same time there is a risk of wasting information that will not be captured by the agent. The limitation is that we have 10 actuators per environment and we need 10 streamed experiences which will be synchronized, so we have to

work with a total of $10n_{\text{environments}}$ set of experiences. A streamed experience consists of a set of states, actions, rewards, and the predicted state that the agent expects to achieve. It is denoted as $(S, A, R, S')_{i,t}$ for each pseudo-environment, and each of the Reynolds numbers under consideration has its own agent and policy.

Previous work on 2D cylinders implemented the various training stages by means of a single-agent reinforcement learning (SARL) configuration. If the action space handles multiple jets at once, as is the case in the present 3D cylinder setup with distributed input forcing and distributed output reward (so-called DIDO scheme), SARL is not a viable option. As opposed to SARL, the MARL framework avoids the curse of dimensionality by exploiting invariances and aims to train local pseudo-environments. Doing so, the high-dimensional control becomes tractable and the agent is trained in smaller domains to maximize the local rewards. Figure 6(b) can help to understand the forthcoming explanation of the MARL setup. All the agents share the same neural-network weights, which is a key factor in significantly accelerating the training process. Note that each agent is coupled to a pair of jets that actuate independently from the others through the training process. The observation state S_i provided to the agent consists of partial pressure values along the domain. This information contains three slices with 99 pressure values each which are aligned with the corresponding jet. The probes or pressure values are concentrated in the wake and near-cylinder regions. This enables the agent to exploit the spanwise pressure gradients.

The total reward $R(t, i_{\text{jet}})$ defined in Equation (6) is expressed as a sum of the local, r^{local} , and global, r^{global} , rewards that correspond to each jet i_{jet} . The heuristic scalar K adjusts the values within the range $[-1, 1]$ and

β balances the local and global rewards; note that a value of $\beta = 0.8$ is used in this work. The rewards r , defined in Equation (7), are functions of the aerodynamic force coefficients C_d and C_l (note that C_{d_b} is the uncontrolled averaged drag in a stationary state). The user-defined parameter α is a lift penalty and in this study we considered $\alpha = 0.6$, which is a good trade-off between ensuring symmetric strategies without excessively restricting the exploration process. The latter is essential to avoid undesired asymmetric strategies which favor a reduction of the component parallel to the incident velocity (drag) towards the perpendicular one (positive or negative lift). This is commonly referred to as the axis-switching phenomenon.

$$R(t, i_{\text{jet}}) = K \left[\beta r^{\text{local}}(t, i_{\text{jet}}) + (1 - \beta) r^{\text{global}}(t) \right], \quad (6)$$

$$r(t, i_{\text{jet}}) = C_{d_b} - C_d(t, i_{\text{jet}}) - \alpha |C_l(t, i_{\text{jet}})|, \quad (7)$$

$$\text{where } C_d = \frac{2F_x}{\rho A_f U_\infty^2} \quad \text{and} \quad C_l = \frac{2F_y}{\rho A_f U_\infty^2}. \quad (8)$$

The aerodynamic forces involve the frontal area $A_f = DL_z$ from the local pseudo-environment surfaces for C_d^{local} and the whole cylinder for C_d^{global} .

The interactions between the agent and the physical environment are denoted as actions A , and they influence the system during T_a time units. We update the jet boundary conditions using Equation (2). The shift in time between actions, $Q_t \rightarrow Q_{t+1}$ is managed through an exponential function. The smooth transition diminishes the appearance of sudden discontinuities which can spoil a training process. The DRL library outputs values in the range of $[-1, 1]$, requiring rescaling as $Q = AQ_{\text{max}}$ to avoid excessively large actuations. Hence, $Q_{\text{max}} = 0.176$ was set based on our experience with DRL for flow control, and corresponds to twice the values used in the 2D cylinder setups [50].

Certain parameters in the DRL configuration are closely tied to the fluid-mechanics problem under consideration. The episode duration is specifically defined to include at least six vortex-shedding periods ($T_k = 1/f_k$). We set $T_a < 0.05T_k$, based on the experience gathered with previous studies [12, 51]. This allows sufficient time between actions to produce an effect on the flow. Note that if the time between actions is too short, there will be noise in the training process and it will become difficult to converge. On the other hand, if this is too large the agent will not be able to control the smaller-scale structures associated with shorter time scales. Thus, a total of 120 actuations per episode is deemed sufficient for evaluating the cumulative reward. It is noteworthy that each episode starts from an uncontrolled converged state of the problem. This corresponds to what happens during training, but when we evaluate the DRL model in exploitation mode (also denoted as a deterministic mode), we make the episodes 4 times longer to ensure statistical convergence.

Note that we also compare the DRL-based control with results from the classical periodic control. The latter is chosen with the same jet flow rate as that of the DRL, and the frequency is chosen based on a parametric analysis of the frequency around the vortex-shedding frequency of the wake. We selected the frequency yielding the highest drag reduction.

Extensive work documented in Ref. [36] was carried out to adjust the MARL framework and the communications setup. For instance, the definition of S is the result of a compromise between computational practicality and physical relevance. The spanwise wavelength of the structures in the wake also helped to define the spacing of the xy planes defining the system state. Note that the number of data points used for this state correlates with the number of weights calculated for the first fully connected layer of

the neural network.

Acknowledgments

This study was enabled by resources provided by the National Academic Infrastructure for Supercomputing in Sweden (NAISS) at PDC, KTH Royal Institute of Technology. R.V. acknowledges financial support from ERC grant no.2021-CoG-101043998, DEEPCONTROL. Views and opinions expressed are however those of the author(s) only and do not necessarily reflect those of the European Union or the European Research Council. Neither the European Union nor the granting authority can be held responsible for them.

Author Contributions

Suárez, P.: Methodology, software, validation, investigation, writing - original draft and visualization. **Álcantara-Ávila, F., Rabault, J., Miró, A. & Font, B. :** Methodology, software, and writing - review & editing. **Lehmkuhl, O. :** Funding acquisition, supervision, and writing - review & editing. **Vinuesa, R.:** Conceptualization, project definition, methodology, resources, writing - original draft, supervision, project administration and funding acquisition.

Data availability

The data and codes used to produce this study will be made available for open access as soon as the article is published.

References

- [1] H. Choi, W.-P. Jeon, J. Kim, Control of flow over a bluff body, *Annual Review of Fluid Mechanics* 40 (2008) 113–139.
- [2] D. P. Raymer, *Aircraft design: A conceptual approach*, AIAA education series, 4th ed., American Institute of Aeronautics and Astronautics, 2006.
- [3] R. T. Whitcomb, A design approach and selected wind tunnel results at high subsonic speeds for wing-tip mounted winglets, Technical Report, NASA IND 8260. Natl. Aeronat. Space Admin, Washington, DC, 1976.
- [4] J. C. Lin, Review of research on low-profile vortex generators to control boundary-layer separation, *Progress in Aerospace Sciences* 38 (2002) 389–420.
- [5] N. Siddiqui, W. Asrar, E. Sulaeman, Literature review: Biomimetic and conventional aircraft wing tips, *International Journal of Aviation, Aeronautics, and Aerospace* 4 (2017) 5–8.
- [6] J. E. Guerrero, D. Maestro, A. Bottaro, Biomimetic spiroid winglets for lift and drag control, *Comptes Rendus Mécanique* 340 (2012) 67–80. Biomimetic flow control.
- [7] R. Vinuesa, S. L. Brunton, B. J. McKeon, The transformative potential of machine learning for experiments in fluid mechanics, *Nature Reviews Physics* 5 (2023) 536–545.
- [8] R. Vinuesa, S. L. Brunton, Enhancing computational fluid dynamics with machine learning, *Nature Computational Science* 2 (2022) 358–366.

- [9] S. Le Clainche, E. Ferrer, S. Gibson, E. Cross, A. Parente, R. Vinuesa, Improving aircraft performance using machine learning: A review, *Aerospace Science and Technology* 138 (2023).
- [10] P. Garnier, J. Viquerat, J. Rabault, A. Larcher, A. Kuhnle, E. Hachem, A review on deep reinforcement learning for fluid mechanics, *Computers & Fluids* 225 (2021) 104973.
- [11] D. Silver, A. Huang, C. J. Maddison, A. Guez, L. Sifre, G. van den Driessche, J. Schrittwieser, I. Antonoglou, V. Panneershelvam, M. Lanctot, S. Dieleman, D. Grewe, J. Nham, N. Kalchbrenner, I. Sutskever, T. Lillicrap, M. Leach, K. Kavukcuoglu, T. Graepel, D. Hassabis, Mastering the game of go with deep neural networks and tree search, *Nature* 529 (2016) 484–503.
- [12] H. Tang, J. Rabault, A. Kuhnle, Y. Wang, T. Wang, Robust active flow control over a range of Reynolds numbers using an artificial neural network trained through deep reinforcement learning, *Physics of Fluids* 32 (2020).
- [13] H. Xu, W. Zhang, J. Deng, J. Rabault, Active flow control with rotating cylinders by an artificial neural network trained by deep reinforcement learning, *Journal of Hydrodynamics* 32 (2020) 254–258.
- [14] R. Paris, S. Beneddine, J. Dandois, Robust flow control and optimal sensor placement using deep reinforcement learning, *Journal of Fluid Mechanics* 913 (2021) A25.
- [15] J. Li, M. Zhang, Reinforcement-learning-based control of confined cylin-

- der wakes with stability analyses, *Journal of Fluid Mechanics* 932 (2022) A44.
- [16] F. Ren, J. Rabault, H. Tang, Applying deep reinforcement learning to active flow control in weakly turbulent conditions, *Physics of Fluids* 33 (2021).
- [17] D. Fan, L. Yang, Z. Wang, M. S. Triantafyllou, G. E. Karniadakis, Reinforcement learning for bluff body active flow control in experiments and simulations, *Proceedings of the National Academy of Sciences* 117 (2020) 26091–26098.
- [18] M. Chatzimanolakis, P. Weber, P. Koumoutsakos, Drag reduction in flows past 2D and 3D circular cylinders through deep reinforcement learning, Preprint arXiv: 2309.02109 (2023).
- [19] R. Vinuesa, O. Lehmkuhl, A. Lozano-Durán, J. Rabault, Flow control in wings and discovery of novel approaches via deep reinforcement learning, *Fluids* 7 (2022) 62.
- [20] W. Chen, Q. Wang, L. Yan, G. Hu, B. R. Noack, Deep reinforcement learning-based active flow control of vortex-induced vibration of a square cylinder, *Physics of Fluids* 35 (2023).
- [21] L. Guastoni, J. Rabault, P. Schlatter, H. Azizpour, R. Vinuesa, Deep reinforcement learning for turbulent drag reduction in channel flows, *European Physical Journal E* 46 (2023) 27.
- [22] X. Yan, J. Zhu, M. Kuang, X. Wang, Aerodynamic shape optimization using a novel optimizer based on machine learning techniques, *Aerospace Science and Technology* 86 (2019) 826–835.

- [23] J. Viquerat, J. Rabault, A. Kuhnle, H. Ghraieb, A. Larcher, E. Hachem, Direct shape optimization through deep reinforcement learning, *Journal of Computational Physics* 428 (2021).
- [24] H. Keramati, F. Hamdullahpur, M. Barzegari, Deep reinforcement learning for heat exchanger shape optimization, *International Journal of Heat and Mass Transfer* 194 (2022) 123112.
- [25] C. Vignon, J. Rabault, J. Vasanth, F. Alcántara-Ávila, M. Mortensen, R. Vinuesa, Effective control of two-dimensional Rayleigh–Bénard convection: invariant multi-agent reinforcement learning is all you need, *Physics of Fluids* 35 (2023).
- [26] M. Kurz, P. Offenhäuser, A. Beck, Deep reinforcement learning for turbulence modeling in large eddy simulations, *International Journal of Heat and Fluid Flow* 99 (2023) 109094.
- [27] G. Novati, H. L. de Laroussilhe, P. Koumoutsakos, Automating turbulence modeling by multi-agent reinforcement learning, *Nature Machine Intelligence* 3 (2021) 87–96.
- [28] A. Beck, M. Kurz, Toward discretization-consistent closure schemes for large eddy simulation using reinforcement learning, Preprint arXiv: 2309.06260 (2023).
- [29] H. J. Bae, P. Koumoutsakos, Scientific multi-agent reinforcement learning for wall-models of turbulent flows, *Nature Communications* 13 (2022) 1443.
- [30] Z. Wang, D. Fan, X. Jiang, M. S. Triantafyllou, G. E. Karniadakis, Deep reinforcement transfer learning of active control for bluff body

- flows at high reynolds number, *Journal of Fluid Mechanics* 973 (2023) A32.
- [31] C. Williamson, Vortex Dynamics in the Cylinder Wake, *Annual Review of Fluid Mechanics* 28 (1996) 477–539.
- [32] D. Barkley, R. D. Henderson, Three-dimensional floquet stability analysis of the wake of a circular cylinder, *Journal of Fluid Mechanics* 322 (1996) 215–241.
- [33] S. L. Brunton, B. R. Noack, Closed-Loop Turbulence Control: Progress and Challenges, *Applied Mechanics Reviews* 67 (2015).
- [34] C. Vignon, J. Rabault, R. Vinuesa, Recent advances in applying deep reinforcement learning for flow control: Perspectives and future directions, *Physics of Fluids* 35 (2023).
- [35] J. Jeong, F. Hussain, On the identification of a vortex, *Journal of Fluid Mechanics* 285 (1995) 69–94.
- [36] P. Suárez, F. Alcántara-Ávila, A. Miró, J. Rabault, B. Font, O. Lehmkuhl, R. Vinuesa, Active flow control for three-dimensional cylinders through deep reinforcement learning, Preprint arXiv: 2309.02462 (2023).
- [37] J. Kim, H. Choi, Distributed forcing of flow over a circular cylinder, *Physics of Fluids* 17 (2005) 033103.
- [38] B. Bays-Muchmore, A. Ahmed, On streamwise vortices in turbulent wakes of cylinders, *Physics of Fluids A: Fluid Dynamics* 5 (1993) 387–392.

- [39] M. S. Bloor, The transition to turbulence in the wake of a circular cylinder, *Journal of Fluid Mechanics* 19 (1964) 290–304.
- [40] G. E. Karniadakis, G. S. Triantafyllou, Frequency selection and asymptotic states in laminar wakes, *Journal of Fluid Mechanics* 199 (1989) 441–469.
- [41] G. E. Karniadakis, G. S. Triantafyllou, Three-dimensional dynamics and transition to turbulence in the wake of bluff objects, *Journal of fluid mechanics* 238 (1992) 1–30.
- [42] C. Norberg, An experimental investigation of the flow around a circular cylinder: influence of aspect ratio, *Journal of Fluid Mechanics* 258 (1994) 287–316.
- [43] M. Vázquez, G. Houzeaux, S. Koric, A. Artigues, J. Aguado-Sierra, R. Arís, D. Mira, H. Calmet, F. Cucchietti, H. Owen, A. Taha, E. D. Burness, J. M. Cela, M. Valero, Alya: Multiphysics engineering simulation toward exascale, *Journal of Computational Science* 14 (2016) 15–27.
- [44] S. Charnyi, T. Heister, M. A. Olshanskii, L. G. Rebholz, On conservation laws of navier–stokes galerkin discretizations, *Journal of Computational Physics* 337 (2017) 289–308.
- [45] S. Charnyi, T. Heister, M. A. Olshanskii, L. G. Rebholz, Efficient discretizations for the EMAC formulation of the incompressible Navier–Stokes equations, *Applied Numerical Mathematics* 141 (2019) 220–233.
- [46] J. Crank, P. Nicolson, A practical method for numerical evaluation of solutions of partial differential equations of the heat-conduction type,

Mathematical proceedings of the Cambridge philosophical society 43 (1947) 50–67.

- [47] F. Trias, O. Lehmkuhl, A self-adaptive strategy for the time integration of Navier-Stokes equations, *Numerical Heat Transfer Part B: Fundamentals* (2011) 116–134.
- [48] M. Schaarschmidt, A. Kuhnle, K. Fricke, TensorForce: A TensorFlow library for applied reinforcement learning, <https://github.com/reinforceio/tensorforce> (2017). Published: Web page.
- [49] J. Schulman, F. Wolski, P. Dhariwal, A. Radford, O. Klimov, Proximal policy optimization algorithms, Preprint arXiv: 1707.06347 (2017).
- [50] P. Varela, P. Suárez, F. Alcántara-Ávila, A. Miró, J. Rabault, B. Font, L. M. García-Cuevas, O. Lehmkuhl, R. Vinuesa, Deep reinforcement learning for flow control exploits different physics for increasing Reynolds number regimes, *Actuators*, MDPI 11 (2022) 359.
- [51] J. Rabault, M. Kuchta, A. Jensen, U. Replade, N. Cerardi, Artificial Neural Networks trained through Deep Reinforcement Learning discover control strategies for active flow control, *Journal of Fluid Mechanics* 865 (2019) 281–302.